Int. J. Solids Structures Vol. 24, No. 1, pp. 51–64, 1988
Printed in Great Britain

0020-7683/88 $3.00 + .00

COLLAPSE OF HYDROSTATICALLY LOADED CYLINDRICAL SHELLS

HENRIK MYHRE JENSEN
Department of Solid Mechanics, Technical University of Denmark, DK-2800, Lyngby, Denmark

(*Received* 3 *September* 1986; *in revised form* 19 *March* 1987)

Abstract—A long circular cylindrical shell subjected to external pressure may collapse through the development of a propagating buckle. In this work a method has been developed for the theoretical prediction of the smallest propagation pressure in the case of path-dependent material descriptions. The method is illustrated by comparing predictions of the propagation pressure based on J_2 flow theory with predictions based on J_2 deformation theory for two different radius to thickness ratios. The modelling is based on thin shell theory and small strain approximations, allowing for large deformations. Results for two different non-linear bending strain measures are compared, and the effect of using a finite strain J_2 flow theory is investigated.

INTRODUCTION

An externally pressurized tube may collapse in a mode in which a buckle will propagate through the entire length of the tube leaving it plastically collapsed (Fig. 1).

Such a collapse has occurred along submarine pipelines. Of particular interest is the smallest propagation pressure P_p at which the velocity of the transition front tends to zero. A theoretical prediction of this pressure in Palmer and Martin[1], $P_p/\sigma_y = (h/R)^2\pi/4$, based on a plastic hinge model somewhat underestimated the experimental results. An experimental study of the problem and related aspects—like buckle arresting—was carried out by Mesloh *et al.*[2] and Johns *et al.*[3]. Kyriakides and Babcock[4 8], Kyriakides and Arikan[9], Kyriakides and Youn[10] and Kyriakides *et al.*[11] carried out detailed experimental studies of several aspects of the propagating buckle problem and have performed theoretical analyses of the large deformation behaviour of inelastic rings under different exterior conditions.

Finally, Chater and Hutchinson[12] linked the ring analysis and the determination of P_p. They argued that one expects every point in the shell material to experience a stress history close to proportional stress development as the transition front passes by. For this reason, deformation theory will essentially describe the inelastic material behaviour. They considered the work balance for steady-state propagation under quasi-static conditions at pressure P_p

$$P_p(\Delta A_D - \Delta A_U) = \Delta W \tag{1}$$

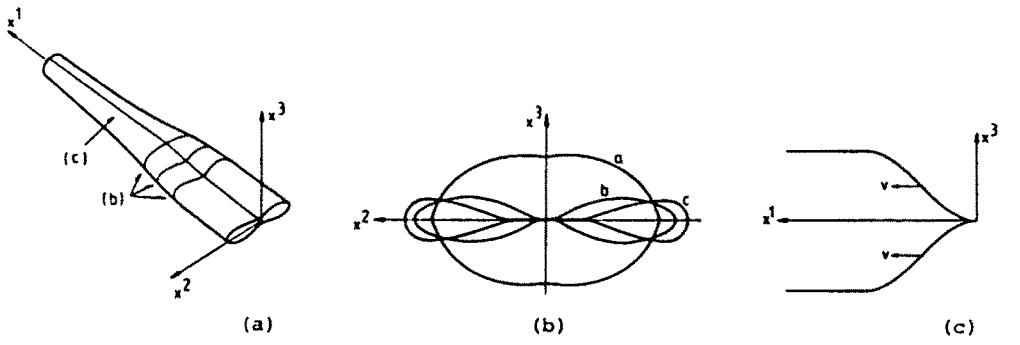

Fig. 1. (a) Mode of collapse for circular cylindrical shell under external pressure, with (b) characteristic cross-sections and (c) generators lying in the vertical plane of symmetry.

in which ΔA_D and ΔA_U denote the area reductions of ring segments far behind and far in front of the transition. Due to the conservativeness of the problem when using deformation theory, the stress work ΔW absorbed by each segment of unit length can be determined by any path bringing the ring from state U to state D. For a tube of infinite length described by deformation theory, these two states are plane strain ring solutions. Now ΔW can most easily be determined from pure plane strain ring deformation as

$$\Delta W = \int_{\Delta A_U}^{\Delta A_D} p(\Delta A)\, \mathrm{d}(\Delta A). \tag{2}$$

Combining eqns (1) and (2) gives a graphical interpretation of P_p on the pressure vs area reduction curve for a ring under plane strain conditions as the level at which the areas above and below this line are equal (Fig. 2).

This Maxwell line construction has been used for other problems concerning propagating instabilities in Chater *et al.*[13] and in Hutchinson and Neale[14].

Comparison with experimental results in Ref. [12] and in Kyriakides *et al.*[15] shows that the method yields accurate results, especially for the thinnest tubes. This is not surprising, since in Refs [12, 15] a small strain, thin ring model is used. Some improvement of the predictions could be expected if ΔW in eqn (2) was determined from the exact three-dimensional theory using a finite strain deformation theory. It is believed that such improvements of the modelling are not relevant until it has been clarified how accurately the deformation theory describes the material behaviour.

The purpose of the present work is to develop a method of predicting P_p, using a path-dependent material model. This requires a description of the complete behaviour during the transition from the unbuckled to the collapsed zone. The modelling is based on thin shell approximations, using small strain material models. As mentioned in Ref. [12], the deformation theory material model must be improved at some level of approximation. The transition front steepens with decreasing radius to thickness (R/h) ratios and at propagation pressures above P_p, which result in large deviations from proportional stressing.

A complete description of the shell behaviour is also required to study the design of buckle arrestors and the initiation of propagating buckles from the local damage of a pipeline.

The method is illustrated by comparing predictions of P_p based on flow theory with predictions based on deformation theory for two shells of different radius to thickness ratios. These comparisons demonstrate the influence of non-proportional stress history, showing that agreement between the predictions confirms the validity of the deformation theory material description.

Results for two different bending strain measures are compared. If the fundamental small strain assumptions are not violated the results should coincide. Therefore, any disagreement gives an impression of the influence of terms that thin shell theory under small strain assumptions do not include.

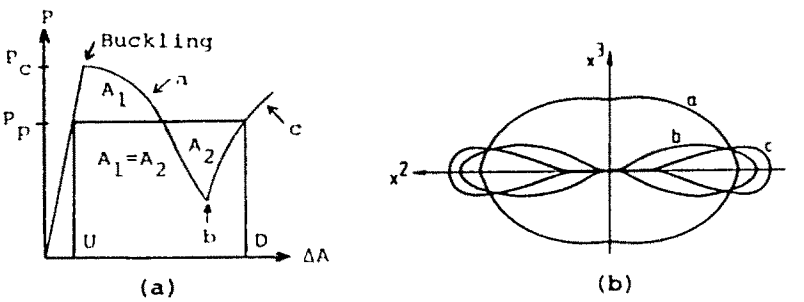

Fig. 2. (a) Graphical construction of P_p from the load vs area reduction curve for a ring under plane strain conditions, with (b) typical stages of deformation indicated.

In the cases considered the strains off the middle surface become quite large. By comparing with results based on a finite strain material model, one gets an impression of the limitations of the small strain material models.

BASIC EQUATIONS

In the following a total Lagrangian description of the fundamental equations is adopted, in which the initial body, with volume V and surface S, is used as a reference. Equilibrium of the deformed state is ensured through fulfilment of the principle of virtual work, which, in the absence of body forces, takes the form

$$\int_V \tau^{ij}\,\delta\eta_{ij}\,\mathrm{d}V = \int_S T^i\,\delta u_i\,\mathrm{d}S \tag{3}$$†

where T^i denotes the surface tractions and u_i the displacements relative to the reference coordinate system. The Lagrangian strain tensor η_{ij} is given by

$$\eta_{ij} = \tfrac{1}{2}(G_{ij}-g_{ij}) \tag{4}$$

in which G_{ij} and g_{ij} are the covariant components of the metric tensors in the deformed and undeformed configurations with determinants G and g. In eqn (3) τ^{ij} denotes the contravariant components of the Kirchhoff stress tensor, related to the Cauchy stresses σ^{ij} by

$$\tau^{ij} = \sqrt{(G/g)}\,\sigma^{ij}. \tag{5}$$

The principle of virtual work is expanded about the current state—not necessarily in equilibrium—giving to lowest order

$$\int_V [\dot\tau^{ij}\,\delta\eta_{ij}+\tau^{ij}\,\delta\dot\eta_{ij}]\,\mathrm{d}V = \int_S \dot T^i\,\delta u_i\,\mathrm{d}S - \left\{\int_V \tau^{ij}\,\delta\eta_{ij}\,\mathrm{d}V - \int_S T^i\,\delta u_i\,\mathrm{d}S\right\} \tag{6}$$

where $\dot{(\ )}$ denotes an incremental quantity. If $\eta = \eta[u_i]$ is a prototype of η_{ij} with $\eta[u_i]$ as a non-linear operator on u_i, $\delta\eta$ denotes the part of $\eta[u_i+\delta u_i]$ which is linear in δu_i, and $\delta\dot\eta$ the part of $\eta[u_i+\dot u_i+\delta u_i]$ which is linear in both $\dot u_i$ and δu_i. Here, δu_i denotes any virtual displacement field fulfilling the kinematical boundary conditions.

In the following we set $\tau^{ij} = \sigma^{ij}$ since the relative volume change $\sqrt{(G/g)}-1$ is entirely due to elastic strains which, by assumption, are small.

The material models to be considered are the classical small strain deformation theory and flow theory with isotropic hardening. In incremental formulation

$$\dot\sigma^{ij} = L^{ijkl}\dot\eta_{kl} \tag{7}$$

the tensor of instantaneous moduli L^{ijkl} takes the following form in the case of deformation theory:

$$L^{ijkl} = \frac{E_s}{1+\nu_s}\left\{\frac{1}{2}(g^{ik}g^{jl}+g^{il}g^{jk}) + \frac{\nu_s}{1-2\nu_s}g^{ij}g^{kl} - \frac{3}{2}\,\frac{E_s/E_t-1}{E_s/E_t-(1-2\nu_s)/3}\,\frac{s^{ij}s^{kl}}{\sigma_e^2}\right\}. \tag{8}$$

Here, E_s denotes the secant modulus on the measured uniaxial stress–strain curve, E_t is the

† Latin letters for indices assume the values 1, 2 and 3, while Greek letters assume the values 1 and 2 only.

tangent modulus and $\nu_s = \nu E_s/E + \frac{1}{2}(1 - E_s/E)$. The stress state is related to the uniaxial stress–strain curve through the effective stress σ_e

$$\sigma_e = \left[\tfrac{3}{2} g_{ik} g_{jl} s^{ij} s^{kl}\right]^{1/2}. \tag{9}$$

The deviator stress tensor is given by

$$s^{ij} = \sigma^{ij} - \tfrac{1}{3} g^{ij} g_{kl} \sigma^{kl}. \tag{10}$$

In the case of flow theory the elastic–plastic moduli takes the form

$$L^{ijkl} = \frac{E}{1+\nu}\left\{\frac{1}{2}(g^{ik}g^{jl} + g^{il}g^{jk}) + \frac{\nu}{1-2\nu} g^{ij}g^{kl} - \chi \frac{3}{2}\frac{E/E_t - 1}{E/E_t - (1-2\nu)/3}\frac{s^{ij}s^{kl}}{\sigma_e^2}\right\} \tag{11}$$

with

$$\chi = \begin{cases} 1, & \text{if} \quad \sigma_e = \sigma_e|_{\max} \quad \text{and} \quad \dot{\sigma}_e > 0 \\ 0, & \text{otherwise.} \end{cases} \tag{12}$$

In the finite strain generalization of eqn (11), relating the Jaumann rate of the Cauchy stress $\overset{\nabla}{\sigma}{}^{ij} = \dot{\sigma}^{ij} + G^{ik}\sigma^{jl}\dot{\eta}_{kl} + G^{jl}\sigma^{ik}\dot{\eta}_{kl}$ to the strain rate $\dot{\eta}_{kl}$, the components of g_{ij} are replaced by G_{ij} in eqns (9)–(11) [16, 17]. In this case, E_t is the tangent modulus on the uniaxial true stress vs natural strain curve.

SHELL EQUATIONS

A simple description of the strain variation through the shell thickness is adopted in accordance with the Kirchhoff–Love hypothesis

$$\begin{aligned} \eta_{\alpha\beta} &= \tfrac{1}{2}(\bar{a}_{\alpha\beta} - a_{\alpha\beta}) - z(\bar{d}_{\alpha\beta} - d_{\alpha\beta}) \\ \eta_{3\alpha} &= 0. \end{aligned} \tag{13}$$

It is assumed that the thickness multiplied by the maximum principal curvature is small compared with unity during all stages of deformation. In eqns (13), $a_{\alpha\beta}$ denotes the metric tensor and $d_{\alpha\beta}$ denotes the curvature tensor of the undeformed middle surface, $(\bar{\ })$ denotes the corresponding quantities on the deformed middle surface, and z is the coordinate along the normal to the middle surface. Furthermore, it is assumed that

$$\sigma^{33} = 0. \tag{14}$$

Combination of eqn (7) and $\dot{\sigma}^{33} = 0$ gives

$$\dot{\eta}_{33} = -L^{33\alpha\beta}\dot{\eta}_{\alpha\beta}/L^{3333}. \tag{15}$$

On the circular cylindrical middle surface with in-plane coordinates $(x, R\phi)$ depicted in Fig. 3, u, v and w denote the axial, circumferential and normal displacements, respectively.

The components of the membrane strain tensor $E_{\alpha\beta} \equiv \frac{1}{2}(\bar{a}_{\alpha\beta} - a_{\alpha\beta})$ (see Niordson[18] for the general expression) take the following form, using $(\ )' = \partial(\ )/\partial x$ and $(\ )^* = \partial(\ )/\partial\phi$

$$\begin{aligned} E_{11} &= u' + \tfrac{1}{2}[(u')^2 + (v')^2 + (w')^2] \\ E_{12} &= \tfrac{1}{2}[u^* k_1 - v' k_2 + w' k_1] \\ E_{22} &= v^*(R - w) - Rw + vw^* + \tfrac{1}{2}[v^2 + w^2 + (u^*)^2 + (v^*)^2 + (w^*)^2] \end{aligned} \tag{16}$$

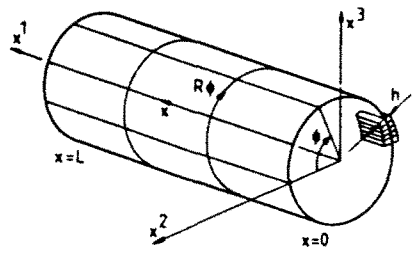

Fig. 3. Coordinate lines on the midsurface of a circular cylindrical shell with radius R, length L and thickness h.

and the components of the curvature tensor take the form (see Appendix)

$$\begin{aligned} \bar{d}_{11} &= u''n_1 + v''n_2 + w''n \\ \bar{d}_{12} &= u^{*\prime}n_1 - k_2'n_2 + k_3'n \\ \bar{d}_{22} &= u^{**}n_1 - k_4n_2 + k_5n. \end{aligned} \tag{17}$$

Here, the following abbreviations are introduced:

$$\begin{aligned} k_1 = 1 + u', \quad k_2 = w - R - v^*, \quad k_3 = w^* + v \\ k_4 = k_2^* + k_1, \quad k_5 = k_1^* - k_2. \end{aligned} \tag{18}$$

The non-dimensional components of the normal to the deformed middle surface are given by

$$\begin{aligned} n_1 &= \bar{a}^{-1/2}[v'k_3 + w'k_2] \\ n_2 &= \bar{a}^{-1/2}[u^*w' - k_1k_3] \\ n &= \bar{a}^{-1/2}[-u^*v' - k_1k_2]. \end{aligned} \tag{19}$$

In eqns (17) it is noted that the terms multiplied by the components of the normal are all linear in the displacements or their derivatives.

In the analysis, the pressure is applied perpendicular to—and measured per unit area of—the deformed middle surface. By this construction, changes in the direction of the normal to the outer surface in comparison with the middle surface normal are neglected, consistent with the Kirchhoff–Love hypothesis. Area changes of the outer surface compared with the middle surface are also neglected, consistent with the assumption that $h\bar{\rho}$ remains small during deformation. Here, $\bar{\rho}$ is the maximum principal curvature.

These relations serve as a basis for the numerical solution of eqn (6), for which the displacements are chosen as independent variables.

NUMERICAL METHOD

Numerical results are obtained representing the axial variation of u, v and w by Hermetian cubics (see for instance Epstein and Murray[19]) within a number of subdivisions of the interval $0 \leqslant x \leqslant L$. Due to the experimentally observed symmetries shown in Fig. 1(b), only a quartersection of the tube need be considered. This circumferential variation in the interval $0 \leqslant \phi \leqslant \pi/2$ is represented by functions fulfilling the symmetry conditions

$$u_0^* = u_{\pi/2}^* = v_0 = v_{\pi/2} = w_0^* = w_{\pi/2}^* = 0. \tag{20}$$

Bifurcations away from this double symmetric mode are not considered. From the experimental results of Ref. [9] such bifurcations do not seem to be relevant at load levels close to the smallest propagation pressure P_p. With the notation

$$\begin{Bmatrix} u \\ v \\ w \end{Bmatrix} = \sum_{n=1}^{N} \begin{Bmatrix} u_n(x)g_n(\phi) \\ v_n(x)h_n(\phi) \\ w_n(x)g_n(\phi) \end{Bmatrix} \tag{21}$$

the following two sets of functions have been compared:

$$g_n(\phi) = \cos 2(n-1)\phi, \quad h_n(\phi) = \sin 2n\phi \tag{22}$$

$$\left.\begin{aligned} g_1(\phi) = 1: \quad g_n(\phi) &= \left(\frac{2\phi}{\pi}\right)^n \left[n+1-n\frac{2\phi}{\pi}\right], \quad n>1 \\ h_n(\phi) &= \left(\frac{2\phi}{\pi}\right)^n \left[1-\frac{2\phi}{\pi}\right] \frac{(n+1)^{n+1}}{n^n} \end{aligned}\right\} \tag{23}$$

in order to study the convergence speed for increasing N in eqn (21). In the cases considered, eqns (22) are normally better choices than eqns (23).

The numerical integration of eqn (6) is performed with 4 Gauss integration points in each axial element, and typically 16 Gauss integration points in the circumferential direction. Through the thickness, Simpson integration is performed using 13 points.

The deformation history is controlled by specifying increments of w at $\phi = \pi/2$. The physical situation we wish to simulate is a volume-controlled experiment, since the pressure reaches several extrema during the deformation history. It is inconvenient to prescribe the volume enclosed by the tube. Since $w(x, \pi/2)$, where x is suitably chosen, increases monotonically for an increasing volume change, it is essentially the same thing to prescribe this quantity. The normal deflection is specified using the Rayleigh–Ritz method, described in Ref. [17].

The principle of virtual work, eqn (6), is solved iteratively at each increment with the tensor of elastic–plastic moduli, eqn (11), kept fixed. If deformation theory is invoked, eqn (8) can be regenerated at each iteration. The configuration-dependent load is included as described in Bathe *et al.*[20] to avoid non-symmetric contributions to the stiffness matrix. Results are compared for the two bending strain measures $K_{\alpha\beta} \equiv d_{\alpha\beta} - \bar{d}_{\alpha\beta}$ and $\bar{K}_{\alpha\beta}$ introduced by Pietraszkiewicz[21], where

$$\bar{K}_{\alpha\beta} = d_{\alpha\beta}(1+E_\gamma^\gamma) - \sqrt{(\bar{a}/a)}\,\bar{d}_{\alpha\beta}. \tag{24}$$

The results based on $\bar{K}_{\alpha\beta}$ are obtained by a Newton–Raphson iteration scheme at each increment using accurate derivatives $\delta\bar{K}_{\alpha\beta}$ and $\delta\dot{\bar{K}}_{\alpha\beta}$. The results based on $K_{\alpha\beta}$ are obtained using approximate derivatives, keeping the normal fixed in eqns (17) between the iterations. Considerable simplifications of the calculations needed to generate the stiffness matrix from eqn (6) are obtained. The number of equilibrium iterations required are practically identical for the two methods.

The stresses are integrated from the previous incremental solution using sub-increments[22, 23]. As noted in Ref. [22], this method can effectively increase the accuracy in cases where the path followed in strain space is less curved than the path in stress space. At the beginning of an incremental solution, the equilibrium states at the three previous increments are used to extrapolate the solution vector containing the nodal degrees of freedom with polynomials of the second degree. This gives a better estimate of the new solution than using the solution at the previous increment, resulting in fewer iterations to reach a given error tolerance.

RESULTS

To test the reliability of the numerical procedure, comparison with recent results for plastic buckling of pressurized circular shells by Huang and Pattillo[24] have been carried

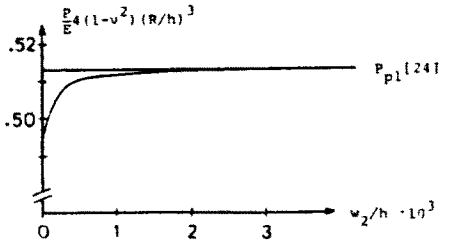

Fig. 4. Comparison of present results with plastic buckling results of Ref. [24]. Here $\nu = 0.3$, $\sigma_y/E = 1.679 \times 10^{-4}$ and $R/h = 8.15$. The present result follows the bifurcation branch with high accuracy.

out. In Fig. 4 the amplitude of w_2 in eqns (21) using eqn (22) is plotted against the pressure for a plane strain ring under external pressure. This mode is identical to the plastic buckling mode of Ref. [24] and has been initiated by superposition of a circumferentially varying load, resulting in an additional deflection of 10^{-5} h.

Of particular interest is a comparison between the present results for ring deformation and those obtained in Refs [12, 15]. Comparing results for increasing N in eqn (21) shows that the convergence speed in the present formulation is strongly dependent on the choice of material parameters. For low hardening materials the ring collapses in a mode in which four plastic hinges form at the symmetry points. Cases where these curvatures are very high, for which the validity of the shell equations becomes doubtful and the convergence with N in eqn (21) is slow, are avoided. The yield stress σ_y and hardening parameter E/E' in a bilinear uniaxial stress–strain curve are chosen so that $N = 6$ in eqn (21) produces a solution in global equilibrium within a few percent. A static analysis of a ring segment gives

$$M_1 - M_0 = (R_0^2 - R_1^2)P/2. \tag{25}$$

The notation is explained in Fig. 5. Within the framework of the analysis, the resultant moments are identified as

$$M = \int_{h/2}^{h/2} g_{22}\sigma^{22} z \, dz. \tag{26}$$

Now, the material parameters are chosen so that eqn (25) is fulfilled by the numerical solution within a few percent when using $N = 6$ in eqn (21).

In Fig. 6 a comparison of the present results and those of Ref. [15] is shown for a rather thick-walled ring ($R/h = 10.5$) using deformation theory and a bilinear uniaxial stress–strain curve with $\sigma_y/E = 1.4 \times 10^{-3}$ and $E/E' = 40$. Here and in the following $\nu = 0.3$.

The small differences in Fig. 6 are believed to be a result of the different models and the different methods of solution.

Convergence towards the results of Ref. [12] can be seen for a ring with $R/h = 40$, $\sigma_y/E = 1.5 \times 10^{-3}$ and a Ramberg–Osgood uniaxial stress–strain curve with strain hardening exponent $n = 10$. Using $N = 6$ in eqn (21) and the set of functions (23) gives $P_p/P_c = 0.269$, while $N = 7$ gives $P_p/P_c = 0.261$. From Fig. 9 in Ref. [12] the value

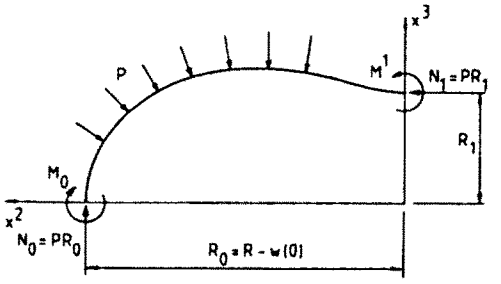

Fig. 5. Quartersection of ring with resultants.

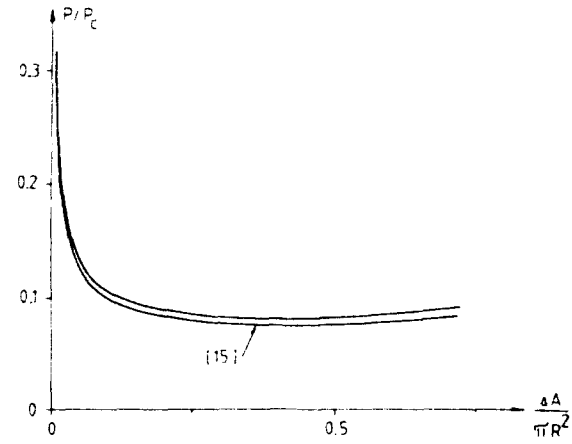

Fig. 6. Comparison of the present analysis for plane strain ring deformation with the results of Ref. [15] for deformation theory. The classical elastic ring buckling pressure is denoted P_c.

$P_p/P_c = 0.25$ is read. In Fig. 7 the gobal equilibrium of the numerical solutions according to eqn (25) are shown for increasing deflections in the case $N = 7$ and for the calculation shown in Fig. 6, which is obtained using $N = 6$ and the set of functions (22).

Figure 7 shows that the result for $R/h = 40$ may still contain some errors due to the discretization, which explains part of the difference in comparison with Ref. [12]. Since the results presented below are in global equilibrium within a higher accuracy than the result, for $R/h = 40$, it is believed that these solutions represent a good accuracy.

Two shells are analysed. Shell I is characterized by the radius to thickness ratio $R/h = 47.4$ and the material parameters $\sigma_y/E = 1.4 \times 10^{-3}$ and $E/E' = 40$. Shell II has $R/h = 14.3$ and the same material parameters as Shell I. The material is fictitious, but the R/h values represent the thinnest and thickest tubes considered in Ref. [12]. The deformation theory predictions of P_p are listed in Table 1.

In these ring calculations the post-touching part of the pressure vs area reduction curve is approximated by a vertical line. This construction, which is analogous to Ref. [12], neglects a small contribution to the area below the P_p line (Fig. 2), resulting in an overestimation of P_p of order 1% according to Ref. [15]. The calculations for Shell II have been repeated for different choices of N and for each of the sets of functions (22) and (23), giving the results listed in Table 2.

These results indicate that eqns (22) are the best choices, but this is not always the case. Comparison of P_p for different shells using the bending strain measures $K_{\alpha\beta}$ and $\bar{K}_{\alpha\beta}$ defined earlier results in changes of P_p below 0.5% in cases where the strains of the middle surface are below 0.5%, as is the case for Shells I and II.

Next, attention will be directed towards the path-dependent material model (11), which requires a description of the transition between the unbuckled and collapsed zone. At the boundary $x = L$ (Fig. 3), the conditions $u = v = w = 0$ are prescribed. At $x = 0$ we prescribe symmetry conditions $u = v' = w' = 0$. These conditions, however, do not affect the value P_p, since this value is characterized as the pressure at which the buckle runs through the pipe without influence from the boundaries.

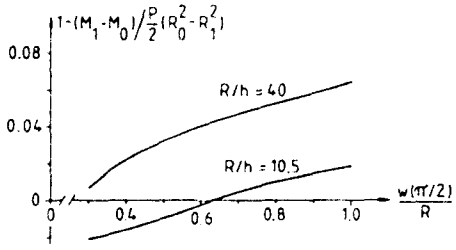

Fig. 7. Overall equilibrium of numerical solutions according to eqn (25).

Table 1. Deformation theory predictions of P_p using eqns (1) and (2) for two shells with geometrical and material data given in the text.

	Shell No. I	Shell No. II
$P_p/\sigma_y \cdot 10^3$	0.512	7.93

Table 2. Comparison of P_p for Shell II with different choices of circumferential discretization

Type of functions	(22)		(23)	
N	6	7	6	7
$P_p/\sigma_y \cdot 10^3$	7.95	7.93	8.11	7.97

A small circumferentially varying load concentrated near $x = 0$ is superposed on the hydrostatic load in order to initiate the buckling mode at pressure P_c. For a shell of infinite length that buckles in the elastic range, the value of P_c is

$$P_c = \frac{E}{4(1-\nu^2)}\left(\frac{h}{R}\right)^3 \tag{27}$$

corresponding to the buckling mode $(u, v, w) = k(0, -\frac{1}{2}\sin 2\phi, \cos 2\phi)$. At increasing deformation, plastic yielding takes place and the ring deformation becomes unstable, the deformation localizes axially. For a shell of finite length, the boundaries initiate the localization mode, which is also utilized by Tvergaard[25] for cylindrical shells under axial compression. This, together with the deformation resulting from the superposed load, ensures the localization takes place at $x = 0$. After this stage of deformation, the superposed load is stepped down to zero and removed over a few increments. In Fig. 8, characteristic stages during deformation are depicted on the load vs volume reduction curve together with the associated shapes of the generator lying in the vertical plane of symmetry.

In the numerical procedure, increments of $w(0, \pi/2)$ are specified until two opposite sides touch each other. Increments of w or w' at $\phi = \pi/2$ are then specified at a point which is not in contact. The contact is maintained by introduction of the boundary conditions $w(x_i, \pi/2) = w'(x_i, \pi/2) = 0$ in the finite element equations. Here, x_i denotes a nodal point in contact. The buckle is allowed to spread through one or two axial elements, which is sufficient for the boundary effects to have died out.

The finite element results for Shells I and II, defined earlier, are shown in Fig. 9, with the results of Table 1 included.

The calculations are carried out with 16 axial elements, which is believed to represent a good accuracy, since an eight element solution differs no more than 0.5% on the pressure–

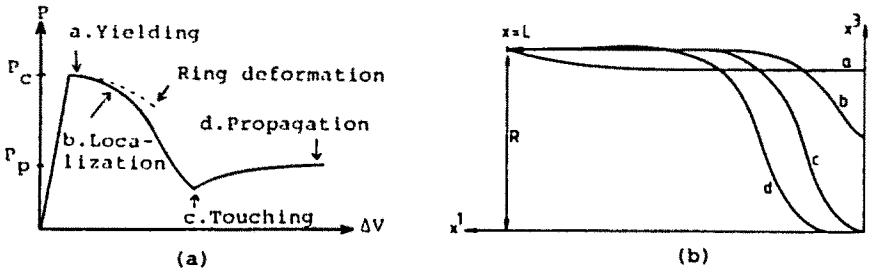

Fig. 8. (a) Load–volume reduction curve for an externally pressurized circular shell that buckles in the elastic range, with (b) characteristic shapes of the generator lying in the vertical plane of symmetry. In order to demonstrate the difference between deformations before and after localization, stage a is exaggerated.

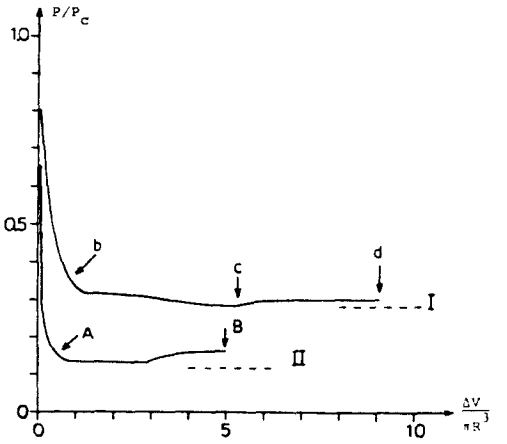

Fig. 9. Load–volume reduction curve for the finite element flow theory calculations using $L = 50R$ for Shell I and $L = 25R$ for Shell II. The deformation theory predictions of P_p are included as broken horizontal lines. The arrows marked b, c and d refer to Fig. 8(b), where the corresponding deformed states are shown. The arrows marked A and B refer to Figs 10(a) and (b), respectively.

volume reduction curve before touching occurs. Obviously, the type of discretization used here is not able to represent the contact forces with very high accuracy. Nevertheless, an eight element deformation theory calculation gives a prediction of P_p only 1.9% above the prediction from the ring analysis for a shell with $R/h = 14.3$.

The flow theory prediction for Shell I is $P_p/\sigma_y \cdot 10^3 = 0.554$. This is 8.2% higher than the deformation theory prediction. For Shell II the flow theory prediction, $P_p/\sigma_y \cdot 10^3 = 10.8$, is 36% higher than the deformation theory prediction listed in Table 1. These results give a quantitative description of the influence of non-proportional stress development as the shell thickness increases. Typical stages of deformation are shown in Fig. 10.

The last part of the pressure–volume reduction curve for Shell II before touching occurs has been repeated, using the bending strain measure $\bar{K}_{\alpha\beta}$, eqn (24). This gives a prediction of the load up to 0.99% lower than that using $K_{\alpha\beta}$. The strains of the middle surface remain below 1% in these cases.

In Fig. 11, the variation of $\eta_{33} = -\Sigma L^{33\alpha\beta}\eta_{\alpha\beta}/L^{3333}$ through the thickness at $\phi = 0$ is shown for Shell II at the final stage of propagation. The results from the ring analysis when touching occurs are included. The strains become quite large in these cases. For this reason it is of relevance to investigate how seriously the small strain assumption affects the results. A simple way to study the effect of performing a three-dimensional analysis, allowing for large strains, is to compare ring deformation results based on small strain flow theory with results based on the finite strain generalization of flow theory. This gives an impression of the limitations of the small strain material models at the strain levels met. Still, the pressure is applied at the midsurface, and the modelling is valid only for deformations fulfilling the Kirchhoff–Love hypothesis and the assumption that $h\bar{\rho}$ is small compared with unity. Here, $\bar{\rho}$ is the maximum principal curvature. For general large strain problems of shells, eqns (13) would normally be rudimentary[26].

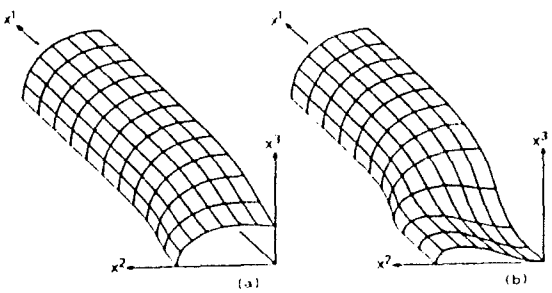

Fig. 10. Coordinate lines on the deformed midsurface at stages A and B marked with arrows in Fig. 9. Due to the symmetries only a quartersection is shown.

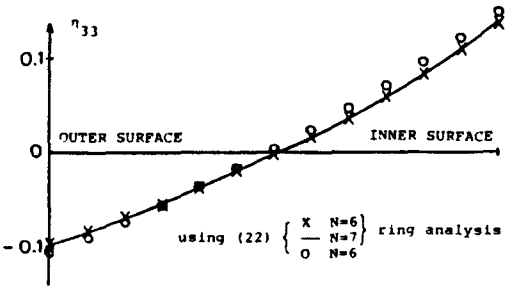

Fig. 11. Variation of $\eta_{33} = -\Sigma L^{33\alpha\beta}\eta_{\alpha\beta}/L^{3333}$ (summation over the increments) through the thickness at $\phi = 0$.

Table 3. Predictions of $P_p/\sigma_y \cdot 10^3$ based on the different material models

	Shell No. I	Shell No. II
Deformation theory, ring analysis	0.512	7.93
Flow theory, finite element analysis	0.554	10.8
Flow theory, ring analysis	0.513	7.98
Finite strain flow theory, ring analysis	0.514	8.88

First, comparison with two of the results in Larsson *et al.*[27] will be shown. The plane strain ring deformation results of Ref. [27] are based on the exact three-dimensional equilibrium equations using a large strain J_2 corner theory material model, which, for a perfect ring, should agree well with the flow theory up to the maximum internal pressure. For the aluminium tubes, the maximum pressure in Ref. [27] is $P'_{max} = 18.0$ MPa for $R/h = 9.5$ and $P''_{max} = 37.9$ MPa for $R/h = 4.5$. The present results using $K_{\alpha\beta}$ are $P'_{max} = 18.6$ MPa and $P''_{max} = 41.4$ MPa when the pressure is referred to the inner surface. Errors of this order of magnitude are expected from the plane stress assumption.

Returning again to the ring calculations for external pressure, the results based on small strain and finite strain flow theory are shown in Table 3. The flow theory and deformation theory predictions mentioned earlier are included for comparison. It will be seen that the results for deformation theory and flow theory in the ring analysis are practically identical. This shows that unloading is not predicted using small strain flow theory. For Shell II the finite strain calculation of P_p is significantly higher than the small strain flow theory prediction of P_p based on the ring analysis. For Shell II the normal strain variation through the thickness at $\phi = 0$ is shown in Fig. 12 when touching occurs. The results can be compared with the small strain results in Fig. 11. The difference is clearly that the neutral axis moves towards the compressed side in the large strain formulation. Associated with this effect, some unloading takes place as the neutral zone moves into material that has previously yielded, which is also noted by Triantafyllidis *et al.*[28]. An accurate modelling of the effect demands a finer discretization than that needed in the small strain calculations, as can be seen from Fig. 12. Since the strains at the midsurface increase

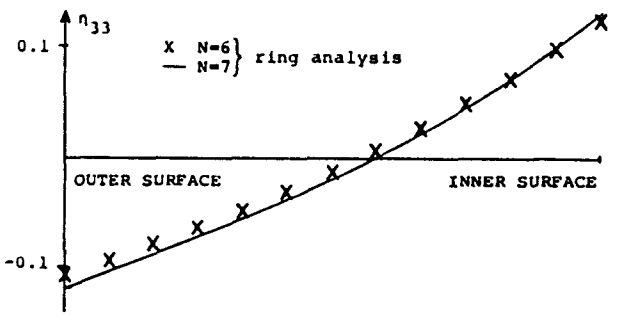

Fig. 12. Variation of $\eta_{33} = -\Sigma L^{33\alpha\beta}\eta_{\alpha\beta}/L^{3333}$ (summation over the increments) through the thickness at $\phi = 0$. The material model is a finite strain flow theory.

as the neutral zone moves away, it is doubtful whether the differences between the material models can be resolved accurately using classical shell theory.

CONCLUSIONS

In the present work, a method for the theoretical prediction of the propagation pressure P_p for circular tubes is presented. The method is valid for general path-dependent elastic–plastic material descriptions. Predictions of P_p based on J_2 deformation theory are compared with predictions based on J_2 flow theory with isotropic hardening. Besides being illustrative for the method, such comparisons are often used to investigate the accuracy of results based on these simple plasticity theories, since experimental results often lie between these theoretical predictions. The comparisons show that over the range of R/h values considered, the predictions of P_p based on flow theory are between 8 and 36% higher than the predictions based on deformation theory. In this range of R/h values, Chater and Hutchinson[12] have compared their deformation theory based predictions of P_p using eqns (1) and (2) with experimental results for aluminium tubes, carried out by Kyriakides. The theoretical results underestimated the experimental values by 2–25%. In the present work, calculations are carried out using material parameters that simulate a higher hardening material than the aluminium specimen, which makes it possible to obtain numerical results of good accuracy with few circumferential expansion functions. A conclusion drawn from convergence studies for ring deformation utilizing the fact that any cross-section of the collapsed tube is very similar to a state of the collapsing ring. In Kyriakides *et al.*[15], theoretical predictions of P_p based on eqns (1) and (2) are compared with experimental results for both aluminium tubes and stainless steel tubes showing that the theoretical method is worse for the higher hardening steel specimen. Making use of this observation when comparing the results of the present work with the results in Chater and Hutchinson[12], the flow theory predictions of P_p seem to be in better agreement with the experiments. This is due to the fact that most of the material points experience a slow and smooth change in the stress path during collapse. It is important, however, to note that the present method of analysis can be used if comparisons with more sophisticated plasticity theories are required.

A first step towards performing a complete three-dimensional finite strain analysis is done, predicting P_p from a finite strain constitutive law with the kinematics still restricted according to the Kirchhoff–Love assumption. It has been verified that such a formulation makes sense by comparing numerical results with results from three-dimensional analyses (see also Jensen[29]). Based on the fact that any cross-section of the collapsed tube is very similar to a state of the collapsing ring, investigating the influence of the small strain assumption on the predictions of P_p can be carried out for the ring collapse. For the thinnest shell considered, the strain levels are below 4% and it has no effect on the calculations when formulating the constitutive law for finite strains. For the thickest tube, the maximum strains are roughly three times greater and the increase in the prediction of P_p using a finite strain constitutive law is 11%. This shows that some improvements of the theoretical predictions based on eqns (1) and (2) are possible, using a three-dimensional finite strain description. But the influence of non-proportional stressing due to axial bending and stretching during collapse cannot be incorporated into eqns (1) and (2). From the results of the present finite element calculations, these effects seem to be important for the problem.

The problem analysed is characteristic in that it involves large deformations including large rotations of an elastic–plastic shell under a configuration-dependent load. To reduce the amount of computational work, the Kirchhoff–Love assumption is introduced and the displacements are expanded in global functions circumferentially rather than using finite elements. Since few calculations of this type exist in the literature, it has been relevant to discuss the verification of the solution strategy and the accuracy of the numerical results. This is done by comparing with earlier reported results and analytical results, by investigating the effect of a finer discretization, by checking that convergence towards identical solutions is observed when different types of expansion functions are used and by checking that a measure for the error in global equilibrium decreases towards zero for increasingly refined discretization. A very efficient verification of the solution strategy and the axial discretization

is to compare predictions of P_p based on eqns (1) and (2) with the finite element calculations of P_p for deformation theory. When using eight axial elements the disagreement in the cases considered is between 0.1 and 1.9%.

In this work, the quantitative influence of several effects on the theoretical prediction of P_p is studied. The results presented are based on a choice of a non-linear large rotation bending strain measure. By checking that results based on an alternative large rotation bending strain measure gives nearly identical predictions, it is thus rendered that the regime of validity for these shell theories is not exceeded.

Acknowledgements—I wish to thank F. I. Niordson and V. Tvergaard for valuable comments on the present work.

REFERENCES

1. A. C. Palmer and J. H. Martin, Buckle propagation in submarine pipelines. *Nature* **254**(5495), 46–48 (1975).
2. R. E. Mesloh, T. G. Johns and J. E. Sorenson, The propagating buckle. *Proc. BOSS 76* **1**, 787–797 (1976).
3. T. G. Johns, R. E. Mesloh and J. E. Sorenson, Propagating buckle arrestors for offshore pipelines. *J. Pressure Vessel Technol.* **100**, 206–214 (1978).
4. S. Kyriakides and C. D. Babcock, On the dynamics and the arrest of the propagating buckle in offshore pipelines. Offshore Technology Conference, OTC 3479, pp. 1035–1045 (1979).
5. S. Kyriakides and C. D. Babcock, On the slip-on buckle arrestor for offshore pipelines. *J. Pressure Vessel Technol.* **102**, 188–193 (1980).
6. S. Kyriakides and C. D. Babcock, Large deflection collapse analysis of an inelastic inextensional ring under external pressure. *Int. J. Solids Structures* **17**, 981–993 (1981).
7. S. Kyriakides and C. D. Babcock, Experimental determination of the propagation pressure of circular pipes. *J. Pressure Vessel Technol.* **103**, 328–336 (1981).
8. S. Kyriakides and C. D. Babcock, Buckle propagation phenomena in pipelines. *Proc. IUTAM Symp. on Collapse*, University College, London, pp. 75–91 (1982).
9. S. Kyriakides and E. Arikan, Postbuckling behaviour of inelastic inextensional rings under external pressure. *J. Appl. Mech.* **50**, 537–543 (1983).
10. S. Kyriakides and S.-K. Youn, On the collapse of circular confined rings under external pressure. *Int. J. Solids Structures* **20**, 699–713 (1984).
11. S. Kyriakides, C. D. Babcock and D. Elyda, Initiation of propagating buckles from local pipeline damages. *J. Energy Resour. Technol.* **106**, 79–87 (1984).
12. E. Chater and J. W. Hutchinson, On the propagation of bulges and buckles. *J. Appl. Mech.* **51**, 269–277 (1984).
13. E. Chater, J. W. Hutchinson and K. W. Neale, Buckle propagation on a beam on a nonlinear elastic foundation. *Proc. IUTAM Symp. on Collapse*, University College, London, pp. 31–41 (1982).
14. J. W. Hutchinson and K. W. Neale, Neck propagation. *J. Mech. Phys. Solids* **31**(5), 405–426 (1983).
15. S. Kyriakides, M.-K. Yeh and D. Roach, On the determination of the propagation pressure of long circular tubes. *J. Pressure Vessel Technol.* **106**, 150–159 (1984).
16. A. Needleman, Bifurcation of elastic–plastic spherical shells subject to internal pressure. *J. Mech. Phys. Solids* **23**, 357–367 (1975).
17. V. Tvergaard, Effect of thickness inhomogeneities in internally pressurized elastic–plastic spherical shells. *J. Mech. Phys. Solids* **24**, 291–304 (1976).
18. F. I. Niordson, *Shell Theory*. North-Holland, Amsterdam (1985).
19. M. Epstein and D. W. Murray, Large deformation in-plane analysis of elastic beams. *Comput. Struct.* **6**, 1–9 (1976).
20. K.-J. Bathe, E. Ramm and E. L. Wilson, Finite element formulations for large deformation dynamic analysis. *Int. J. Numer. Meth. Engng* **9**, 353–386 (1975).
21. W. Pietraszkiewicz, Lagrangian description and incremental formulation in the non-linear theory of thin shells. *Int. J. Non-linear Mech.* **19**(2), 115–140 (1983).
22. D. Bushnell, A strategy for the solution of problems involving large deflections, plasticity and creep. *Int. J. Numer. Meth. Engng* **11**, 683–708 (1977).
23. V. Tvergaard, Creep-buckling of rectangular plates under axial compression. *Int. J. Solids Structures* **15**, 441–456 (1979).
24. N. C. Huang and P. D. Pattillo, Inelastic buckling of cylindrical shells subjected to axial tension and external pressure. *AIAA J.* **21**(10), 1477–1478 (1983).
25. V. Tvergaard, On the transition from a diamond mode to an axisymmetric mode of collapse in cylindrical shells. *Int. J. Solids Structures* **19**, 845–856 (1983).
26. J. G. Simmonds, The strain energy density of rubber-like shells. *Int. J. Solids Structures* **21**, 67–77 (1985).
27. M. Larsson, A. Needleman, V. Tvergaard and B. Storåkers, Instability and failure of internally pressurized ductile metal cylinders. *J. Mech. Phys. Solids* **30**(3), 121–154 (1982).
28. N. Triantafyllidis, A. Needleman and V. Tvergaard, On the development of shear bands in pure bending. *Int. J. Solids Structures* **18**, 121–138 (1982).
29. H. M. Jensen, Tube collapse due to external pressure. *Proc. Int. Conf. Computational Plasticity*, Barcelona, Spain (April 1987).

APPENDIX

Due to Ref. [21], the components of $\sqrt{(\bar{a}/a)}\bar{d}_{\alpha\beta}$ are generally given by

$$\sqrt{(\bar{a}/a)}\bar{d}_{\alpha\beta} = -(D_\beta m^\lambda - d^\lambda_\beta m)L_{\lambda\alpha} - (d_{\alpha\beta}m^\lambda + m_{,\beta})\phi_\alpha. \tag{A1}$$

Here

$$m^\lambda = -(1+\theta^\mu_\mu)\phi^\lambda + \phi_\alpha(\theta^{\mu\lambda} - \omega^{\mu\lambda}) \tag{A2}$$

$$m = 1 + \theta^\lambda_\lambda + \tfrac{1}{2}\theta^\lambda_\lambda\theta^\mu_\mu - \tfrac{1}{2}\theta^\lambda_\mu\theta^\mu_\lambda + \phi^2 \tag{A3}$$

$$L_{\alpha\beta} = a_{\alpha\beta} + \phi_{\alpha\beta}, \quad \phi_{\alpha\beta} = D_\alpha u_\beta - d_{\alpha\beta}w \tag{A4}$$

$$\omega_{\alpha\beta} = \tfrac{1}{2}(D_\alpha u_\beta - D_\beta u_\alpha), \quad \theta_{\alpha\beta} = \tfrac{1}{2}(D_\beta u_\alpha + D_\alpha u_\beta) - d_{\alpha\beta}w \tag{A5}$$

$$\phi_\alpha = w_{,\alpha} + d^\beta_\alpha u_\beta, \quad \phi = \tfrac{1}{2}\varepsilon^{\alpha\beta}D_\beta u_\alpha \tag{A6}$$

where $(\ )_{,\alpha}$ and $D_\alpha(\ )$ denote partial and covariant differentiation, respectively. The skew-symmetric surface permutation tensor is denoted $\varepsilon^{\alpha\beta}$. For the cylindrical middle surface in Fig. 3, $u_1 = u$ and $u_2 = Rv$. In this case the components of $\bar{d}_{\alpha\beta}$ take the form of eqns (17).